CrossMark

Numerical study on rotordynamic coefficients of the seal of molten salt pump

Yao-Yu Hu[1] · De-Zhong Wang[1] · Yuan Fu[2] · Jun-Lian Yin[1]

Abstract Molten salt pump is applied to pump high-temperature molten salt as the primary coolant of a molten salt reactor. The pump, generally a vertical rotor system, suffers from radial force generated by the liquid seal component, and the rotordynamic characteristics of the pump are affected considerably. In this paper, the rotordynamic coefficients of the tooth-on-stator liquid seal in molten salt pump are studied. The flow in the seal region is simulated using computational fluid dynamics technique. Parameters of the inlet loss and the pre-swirl at the inlet region of the seal are calculated. The coefficients of resistance and the wall parameters are obtained from the simulation results by data fitting method. The rotordynamic coefficients are analyzed based on the bulk-flow model of liquid seal. The rotordynamic characteristics, with and without the liquid seal, of the objective molten salt pump are inspected. The first critical speed of the rotor is found to increase. Harmonic analysis shows that the pump, being sensitive to unbalance force though, can operate safely under its design specifications.

Keywords Molten salt pump · Liquid seal · Rotordynamic coefficient · Rotordynamics

✉ De-Zhong Wang
   dzwang@sjtu.edu.cn

1   School of Mechanical Engineering, Shanghai Jiao Tong University, Shanghai 200240, China

2   Shanghai Institute of Applied Physics, Shanghai 201800, China

1 Introduction

In a molten salt reactor (MSR), high-temperature molten salt mixture is used as the primary coolant, and reactor coolant pumps are used to convey the molten salt to the reactor core and transport the enormous heat generated by the core.

The objective molten salt pump is a vertical pump, with a motor on the top and the impeller at the bottom. There is a set of liquid seals between the impeller and the supporting bearings. The seals and impeller are immersed in the molten salt. The molten salt in the clearance of the seals exerts lateral force to the pump rotor under normal operation condition, as a result of whirl motion of the rotor. Rotordynamics characteristics of the rotor system are vulnerable to this lateral force because the pump possesses a cantilever configuration with the impeller mounted out of the supporting range of the bearings. Thus, accurate rotordynamics analysis is indispensable before field deployment to ensure safety. A key issue to the rotordynamics analysis is the evaluation of the fluid induced forces stem from the seals. The forces may destabilize the pump rotor and narrow the safety margin, or by contrast, stabilize the pump rotor by providing the system with damping effect. The fluid induced forces are typically modeled as rotordynamic coefficients.

Generally, the lateral force of fluid in the seal is decomposed into the radial force, f_n, and the tangential force, f_t. The projection of f_n and f_t in the stationary coordinates XOY onto the X- and Y-axes can be expressed as F_X and F_Y, respectively. The force components F_X and F_Y are often described by a set of rotordynamic coefficients with linear relationship.

 Springer

$$\begin{Bmatrix} F_X \\ F_Y \end{Bmatrix} = - \begin{bmatrix} M & m \\ -m & M \end{bmatrix} \begin{Bmatrix} \ddot{X} \\ \ddot{Y} \end{Bmatrix} - \begin{bmatrix} C & c \\ -c & C \end{bmatrix} \begin{Bmatrix} \dot{X} \\ \dot{Y} \end{Bmatrix} \\ - \begin{bmatrix} K & k \\ -k & K \end{bmatrix} \begin{Bmatrix} X \\ Y \end{Bmatrix}, \tag{1}$$

where M, C and K denote the direct added mass, damping and stiffness coefficients, respectively, while the lowercase m, c and k are the cross-coupled counterparts.

The work of Fritz [1, 2] and Childs [3] forms the foundation to study rotordynamic coefficients. In theoretical researches, the fluid flow in the seals is usually simplified from three-dimensional flow into the two-dimensional space. Besides, it is assumed that the flow is fully developed. Childs [3] obtained the rotordynamic coefficients based on the bulk-flow theory of Hirs [4]. The bulk-flow theory is based on the experimental evidence of the relation between the shear stress on the walls and the average velocity of the fluid confined in the clearance. The bulk-flow model can be expressed as

$$\frac{\tau_{\mathrm{w}}}{\frac{1}{2}\rho u_{\mathrm{m}}^2} = n_0 \left(\frac{\rho u_{\mathrm{m}} H}{\mu} \right)^{\mathrm{m}_0}, \tag{2}$$

where τ_{w} is the wall shear stress; u_{m} is the average velocity; H is the nominal clearance; ρ and μ are density and dynamic viscosity of the working fluid, respectively. Due to various geometries and operation conditions, experimental tests of the seal or computations are needed to address a set of wall coefficients, n_0 and m_0, which are assumed to be constant throughout the subsequent analysis. Childs [3] simplified the 3-D fluid dynamics equations into 2-D version by using the bulk-flow model and obtained rotordynamic coefficients of a finite length plain annular seal after a perturbation analysis.

However, for seals of complex geometries, such as labyrinth seals and honeycomb seals, it is difficult to develop a theoretical model for such complex flow regions. Rhode et al. [5], Athavale et al. [6], Moore et al. [7, 8], and Untaroiu et al. [9] used computational fluid dynamics (CFD) technique to evaluate the radial forces in liquid seals. This kind of CFD study should be conducted on several whirl frequencies at every interested rotating speed of the rotor. In the rotordynamic and safety analysis of pumps, the rotordynamic coefficients for a wide range of rotating speeds are required in advance.

Childs et al. [10] showed that the flow resistance in the liquid seal, where the wall geometries are no longer plain or smooth, exhibited characteristics similar to the plain annular seal. They obtained a set of wall coefficients analogous to the n_0 and m_0 in Eq. (2). Then the complex 3-D flow field was studied by simplified two-dimensional equations based on the bulk-flow model. Similar theory was used and associated computer code was developed by Kleynhans et al. [11]. This code was continuously tested against experimental data of various types of seals [12, 13].

In this paper, the liquid seal in molten salt pump together with the seal inlet region are simulated by CFD techniques. The inlet loss and the pre-swirl coefficients of the specific seal configuration are obtained. Successive CFD simulations on the seal reveal the wall coefficients, which are the preliminary input parameters of Childs' method in cooperation with the bulk-flow model. Then, the rotordynamic coefficients are acquired based on the bulk-flow model of liquid seal. Finally, the rotordynamic characteristics of the molten salt pump are inspected.

2 Wall coefficients and seal resistance

The liquid seal is at the impeller back. Figure 1 shows location and geometry of the liquid seal in the molten salt pump.

There are triangle-shaped circumferential slots along the axial direction of the pump rotor, hence the seal of the tooth-on-stator configuration. The geometry parameters (in mm) include: tooth–head distance $p_{\mathrm{t}} = 2.9$, tooth–root distance $p_{\mathrm{b}} = 2.9$, nominal clearance $H = 0.75$, distance between tooth–root and rotor $H_{\mathrm{b}} = 3.42$, rotor radius $r = 42.5$ and length of seal $L = 43.5$. The molten salt flows through the clearance of seal under the pressure difference between the back region of the impeller and the seal outlet. The pressure loss is expressed as

$$\Delta p = (1 + \xi + 2\sigma_{\mathrm{c}}) \frac{\rho V_{\mathrm{s}}^2}{2}, \tag{3}$$

where Δp is the pressure loss, V_{s} is the average axial velocity of the bulk of fluid in the clearance, ξ describes pressure loss of the fluid squeezing into a relatively narrow field from a wide space and σ_c is resistance coefficient of the liquid seal. According to Childs et al. [10], σ_{c} can be evaluated by averaging σ_{s} and σ_{r}, where σ_{s} is a correction coefficient and σ_{r} is the resistance coefficient of the plain annular seal with the similar geometrical configuration to the tooth-on-stator liquid seal. The above relationship can be written as Eqs. (4)–(7).

$$\sigma_{\mathrm{c}} = \frac{1}{2}(\sigma_{\mathrm{r}} + \sigma_{\mathrm{s}}), \tag{4}$$

$$\Delta p_{\mathrm{r}} = (1 + \xi + 2\sigma_{\mathrm{r}}) \frac{\rho V_{\mathrm{r}}^2}{2}, \tag{5}$$

$$\sigma_{\mathrm{r}} = n_{\mathrm{r}} R a_{0,\mathrm{r}}^{\mathrm{m}_{\mathrm{r}}} \left[1 + \frac{1}{4b_{\mathrm{r}}^2} \right]^{\frac{1+m_{\mathrm{r}}}{2}} \frac{L}{H}, \tag{6}$$

Fig. 1 Location (a) and geometry (b) of the liquid seal
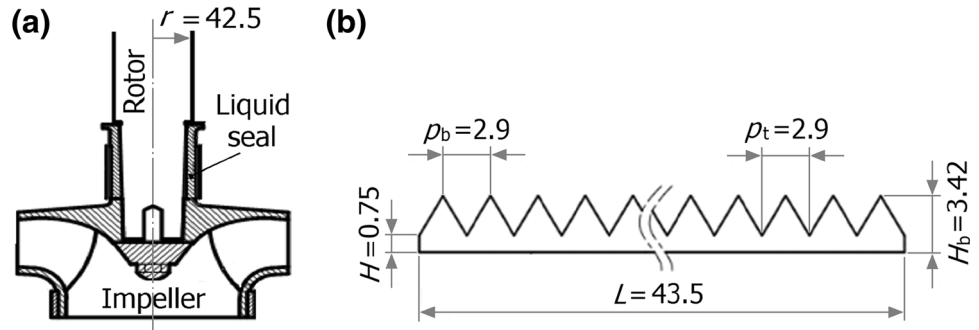
$$\sigma_s = n_s Ra_{0,s}^{m_s} \left[1 + \frac{1}{4b_s^2}\right]^{\frac{1+m_s}{2}} \frac{L}{H}, \tag{7}$$

where V_r is average axial velocity of the fluid in the plain annular seal; L is length of the liquid seal; $Ra_{0,r}$ and $Ra_{0,s}$ are the axial Reynolds numbers of the plain annular seal and the tooth-on-stator liquid seal, respectively.

$$Ra_{0,r} = \frac{2\rho V_r H}{\mu} \tag{8}$$

$$Ra_{0,s} = \frac{2\rho V_s H}{\mu} \tag{9}$$

In Eqs. (6) and (7), the coefficients m_s, n_s, m_r and n_r are the four wall coefficients which are analogous to the m_0 and n_0 coefficients in Eq. (2). The rotordynamic coefficients can be estimated by the methodology developed by Childs et al. [10] after the four wall coefficients are determined. The b_r and b_s in Eqs. (6) and (7) are the ratios of average axial velocities to surface velocity of the rotating rotor, written as Eq. (10), where ω is rotating speed of the rotor,

$$b_r = V_r/(r\omega), b_s = V_s/(r\omega). \tag{10}$$

Certain procedures should be followed to evaluate the wall coefficients, m_s, n_s, m_r and n_r. The resistance coefficient σ_r is obtained from Eq. (5) with the plain annular seal. The σ_c is measured by Eq. (3) on the actual tooth-on-stator liquid seal. The σ_s is calculated by Eq. (4). The previous steps should be repeated until several sets of resistance coefficients are obtained. With over two sets of σ_r and σ_s, m_s, n_s, m_r and n_r can be evaluated by fitting Eqs. (6) and (7) with the least-square method.

3 Flow simulation

Generally, the resistance coefficients σ_r and σ_c, the inlet loss coefficient ξ are obtained from experiments. However, it is difficult to test the actual molten salt pump since the fluid is of high temperature. Besides, a plain annular seal, which is not installed on the pump, should be made so as to evaluate σ_r by testing. The CFD technique is adapted in this

study to evaluate the resistance coefficients and the inlet loss coefficient. Similar approach was performed by Migliorini et al. [14], who simulated properties of the base flow inside the seal by CFD technique. Further, the rotordynamic coefficients are calculated based on the bulk-flow model.

3.1 Inlet loss and pre-swirl coefficient

For calculating the inlet loss coefficient, the flow region spanning from the impeller outlet to the liquid seal inlet shall be modeled. The molten salt of relatively higher pressure at the impeller outlet flows through the impeller back (Fig. 2a) squeezes into the seal inlet region (while the pressure decreases) and flows along axial direction inside the liquid seal (while the pressure drops continuously until the molten salt reaches the seal outlet).

The flow region is divided into two fluid domains in the model as described in Fig. 2b. Domain A is the flow field across the impeller back, while Domain B is the molten salt in the seal clearance. The flow region is divided into two parts in favor of lowering the meshing difficulty. In the following section, wall coefficients are evaluated by simulations only on the grid of Domain B. The exchange of fluid properties between the two domains is realized by the interface functionality provided by the CFX software. One-fourth of the whole flow region is modeled since the fluid field is circumferentially symmetric. A set of periodic interfaces are utilized on the sides of the domains in the circumferential direction.

The inlet boundary condition of the whole computational model is set to be opening. This is because that certain level of recirculation flow will be present near the outer tip of the impeller when it rotates. The opening pressure is 0.4 MPa. The outlet boundary condition is average static pressure, 0 Pa. These boundaries allow us to determine the mass flow rate through the liquid seal at the design point. The rotor wall is set to be rotating wall in the stationary coordinate frame with the angular velocity equaling the speed of the rotor. The stator wall is set as stationary wall. Both the rotor wall and stator wall are
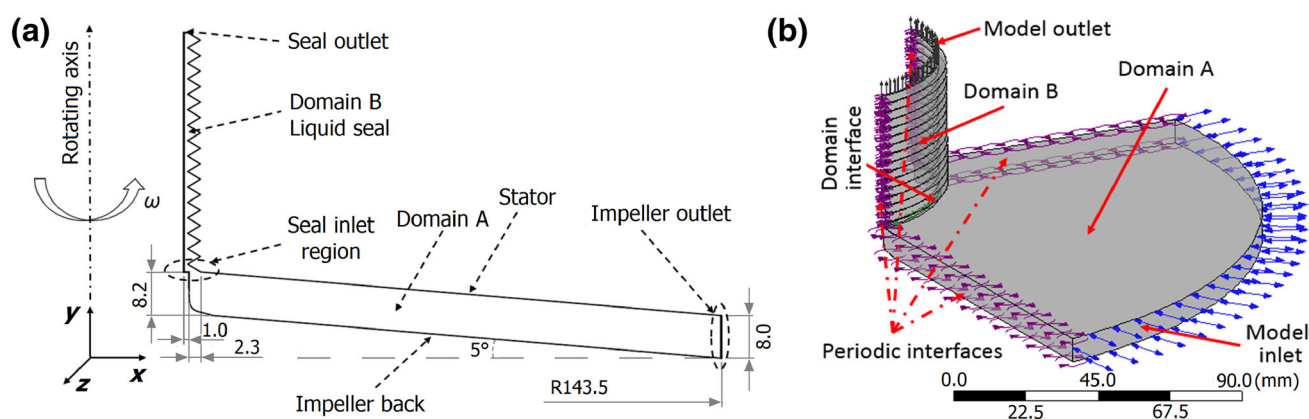
Fig. 2 Schematics (dimensions in mm) of the liquid seal with impeller back region (**a**) and the simulation model (**b**)

configured as smooth walls. The working fluid is LiF–BeF$_2$, a common molten salt [15]. The molten salt inside the seal clearance is assumed to have uniform temperature (700 °C). The density and the viscosity of LiF–BeF$_2$ are assumed to be constants. Table 1 shows the simulation parameters. Steady-state simulations are performed on the model. The torque on the rotor surface along the rotation axis, the radial force on the rotor and the average axial velocity at the outlet of the seal are monitored in the simulation.

Because of the rotor rotation, strong shear flow may exist in the narrow clearance of the seal. For a proper simulation of the flow in the liquid seal, shear stresses in the vicinity of the rotating and stationary walls should be accurately calculated. The SST k-ω turbulent model with automatic wall function is adopted [9].

The two domains in Fig. 2 are discretized and meshed into hexahedral grids by the ICEM software. Three grids are generated for the grid convergence test. Table 2 shows detailed information about the grids termed as the coarse, medium and fine grid according to the numbers of elements. The grids are prepared in the manner recommended by Celik et al. [16]. Thus, while the numbers of elements increase among the grids, the average element lengths should decrease with the same ratios. The grid convergence test can be performed with the average element lengths and

representative physical properties obtained from the simulations [16]. The elements near the seal walls of all the three grids are carefully distributed, making the y^+ values of the near wall elements to be close to 1.

The outlet mass flow rate, the torque on the seal rotor surface and the resistance coefficient are the physical properties employed in the grid convergence test (Fig. 3). Following the procedures proposed by Celik et al. [16], the order of convergence (p_c), the approximate relative error (e_a), the extrapolated relative error (e_{ext}) and the grid convergence index (GCI) are evaluated using the mass flow rate and the σ_c values, as listed in Table 3. It can be seen that the σ_c values have larger GCI values. In order to check the grid dependence of the simulations, the values in Table 3 are supplied into Eq. (11), where r_{21} is the ratio of the average grid lengths of the fine and medium grids. The value obtained by Eq. (11) is approximately unity. This indicates that the simulations can be thought to be in the asymptotic range of convergence. The torque values, being too close to each other, are inapplicable for the evaluation procedures. This indicates that the grid independent solutions are already attained. The fine grid is adopted in the following numerical simulations.

$$\frac{\text{GCI}_{\text{medium}}}{r_{21}^{p_c}\text{GCI}_{\text{fine}}} = \frac{10.3\%}{1.277^{0.78} \cdot 8.37\%} \approx 1.017 \qquad (11)$$

The velocity vectors projected onto the meridian plane are shown in Fig. 4a. It can be seen that the molten salt squeezes into the clearance at the seal inlet region. Consequently, the average velocity increases remarkably and the pressure drops. Figure 4b shows a sudden pressure drop (Region a) right after the fluid flows into the seal. However, the pressure increases (Region b) slightly before decreasing to the pressure predefined at the seal outlet.

As shown in Fig. 4b, the total pressure drop from the impeller outlet to the seal outlet consists of three parts: Part A, the pressure loss between the impeller outlet and the liquid seal inlet, due to friction; Part B, the pressure drop at

Table 1 Simulation parameters

Items	Value
Inlet pressure (MPa)	0.4
Outlet pressure (MPa)	0
Rotor angular velocity, ω (rad/s)	151.8
Residual convergence criteria (RMS*)	1×10^{-5}
Density of the molten salt, ρ (kg/m^3)	1940
Dynamic viscosity of the molten salt, μ (Pa s)	0.0056

RMS Root mean square

Table 2 Grid information

Items	Value		
	Coarse	Medium	Fine
Number of elements in Domain A, ($\times 10^6$)	0.394	0.798	1.674
Number of elements in Domain B, ($\times 10^6$)	1.459	2.880	5.983
Average element length, ($\times 10^{-4}$ m)	4.05	3.22	2.53
Height of first elements on rotating wall in Domain B, ($\times 10^{-6}$ m)	1		
Height of first elements on stationary wall in Domain B, ($\times 10^{-6}$ m)	1		
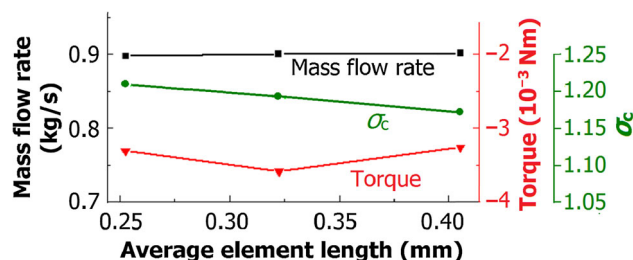
Fig. 3 Grid convergence test

Table 3 Grid convergence test result

| Physical property	Grid	p_c	e_a (%)	e_{ext} (%)	GCI (%)
Mass flow rate	Medium	2.87	0.12	0.12	0.16
	Fine		0.27	0.26	0.32
σ_c	Medium	0.78	1.60	7.59	10.3
	Fine		1.40	6.27	8.37

the seal inlet region, due to sudden squeezing of the fluid; and Part C, the pressure drop inside the seal clearance, due to friction. It can be assumed that the pressure drop of Part A is included in Part B. This means that the friction pressure drop in the fluid flowing along the back of impeller, Part A, can be described by ξ, which is expressed by Eq. (12), letting $\sigma_c = 0$ in Eq. (3).

$$\xi = \frac{2\Delta p_{AB}}{\rho V_s^2} - 1 \tag{12}$$

where Δp_{AB} is the sum of pressure drops of Parts A and B, and V_s is evaluated at the seal inlet region in Fig. 4. The result is $\xi = 0.14$. Thus, the friction pressure drop inside the actual seal region, Part C, can be obtained from the total pressure drop between the impeller outlet and the seal outlet by using Eq. (3). Some authors had their inlet pressure loss coefficient of 0.1 [17, 18], while others took 0.5 as value of ξ [19, 20]. Therefore, our ξ value lies reasonably within the valid range.

It is observed that the molten salt gains circumferential velocity from the shear force on the back surface of the rotating impeller, making the molten salt rotate before entering the liquid seal region. Figure 5 shows the circumferential velocity along a radial line at the seal inlet region in Fig. 4a. The radial location and circumferential velocity are converted into their dimensionless versions, $\bar{r}$
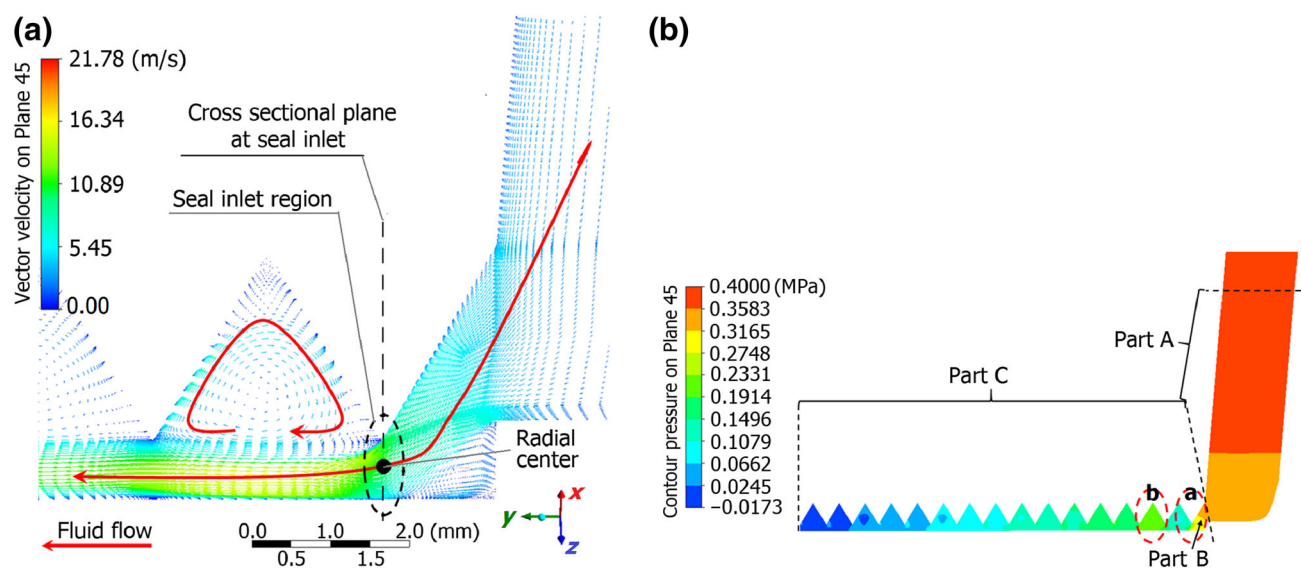
Fig. 4 Velocity vectors projected onto the meridian plane (**a**) and pressure field along axis (**b**)

and $\bar{V}_{cir}$, respectively. Radial location $\bar{r} = 0$ at the rotor surface, when 1 means the tooth tip on the stator. The circumferential velocity can be non-dimensionalized by tangential velocity of the rotor surface and averaged by Eq. (13). We have $\bar{V}_{cir,a} = 0.99$, which will be used in calculating the pre-swirl coefficient.

$$\bar{V}_{cir,a} = \frac{\int_0^1 \bar{V}_{cir}(\bar{r})\mathrm{d}\bar{r}}{\int_0^1 \mathrm{d}\bar{r}} \tag{13}$$

The above simulation also gives the mass flow rate at the outlet of the liquid seal, which is about 0.9 kg/s for the one-fourth portion of the actual fluid field. This value will be used in the following computations.

3.2 Wall coefficients analysis

CFD computations are done on both the actual tooth-on-stator liquid seal and the imaginary plain annular seal in Fig. 1b to get m_s, n_s, m_r and n_r. Ten simulation cases are performed to estimate the wall coefficients. Five of them use the grid of Domain B in Fig. 2b. The others are performed on the mesh of Model (b) in Fig. 1b, meshed separately following the same criterion applied to Domain B.

Simulations of the two configurations of seals are performed with the same boundary conditions. The mass flow rates are predefined at the seal inlets. The mass flow rate of the one-fourth portion under the designed pressure drop is about 0.9 kg/s, which is used as the central value for the simulations from 0.45 to 1.35 kg/s. We note that the inlet boundary conditions of the CFD simulations in the previous section are static pressure, but the mass flow rate boundary conditions are used in the present simulations. The simulation is more stable with this boundary condition, because it prevents disturbance from the reverse flow near the rotor surface. Zero static pressure is specified as the

outlet boundary condition for all the simulations. The rotating speed of the rotor wall is 151.8 rad/s along the rotor axis. All other surfaces on the stator are defined as stationary smooth wall.

Again the k–ω SST turbulent model is adopted. The settings of the convergence monitor and the physical properties of the molten salt are the same as those listed in Table 1. The calculated average axial flow velocity and the pressure drop are listed in Table 4. As expected, the tooth-on-stator liquid seal has larger pressure drop and exhibits higher flow resistance than the plain annular seal does. This phenomenon can be illustrated with the resistance coefficient σ_r and σ_c in Fig. 6, where σ_c is generally 50 % higher than σ_r. Here, σ_r and σ_c are calculated by Eqs. (14) and (15) using the CFD results of the plain annular seal and the tooth-on-stator liquid seal, respectively. As mentioned in the previous section, the inlet pressure loss is excluded from the pressure drop. The pressure drop is only attributed to the friction inside the seal clearance.

$$\Delta p = \sigma_r \rho V_r^2 \tag{14}$$

$$\Delta p = \sigma_c \rho V_s^2 \tag{15}$$

The wall coefficients m_r and n_r are determined by curve fitting method. The wall coefficients m_s and n_s are calculated by fitting with σ_s which is obtained by Eq. (4). The results are $m_r = -0.3895$, $n_r = 0.3249$, $m_s = 0.0530$ and $n_s = 0.0173$. Figure 7 shows the σ_c values calculated using CFD and predicted by Eqs. (4), (6) and (7) using the wall coefficients m_r, n_r, m_s and n_s. The coherence of the two curves indicates that the wall coefficients give acceptable approximation of the flow resistance characteristics within certain leakage range around the design point.

4 Procedures of rotordynamic coefficients analysis

Using the wall coefficients, the rotordynamic coefficients of the liquid seal can be estimated in three steps.

(1) The inlet loss coefficient (ξ) and inlet circumferential velocity ($\bar{V}_{cir,a}$) determined in the previous sections are assumed to be constant throughout the subsequent process. The pre-swirl coefficient v_0 defined by Childs et al. [10] is used. It is related to the CFD result by

$$\bar{V}_{cir,a} = \frac{1}{2} + v_0. \tag{16}$$

(2) The procedure developed by Childs et al. [10] includes solving a 2-D and a 1-D ordinary differential equation sets with predefined boundary conditions. The 1-D equation set is for the zeroth-order flow field. The other is for the perturbed first-order flow field as consequence of the rotor whirl motion. The first-order equations developed
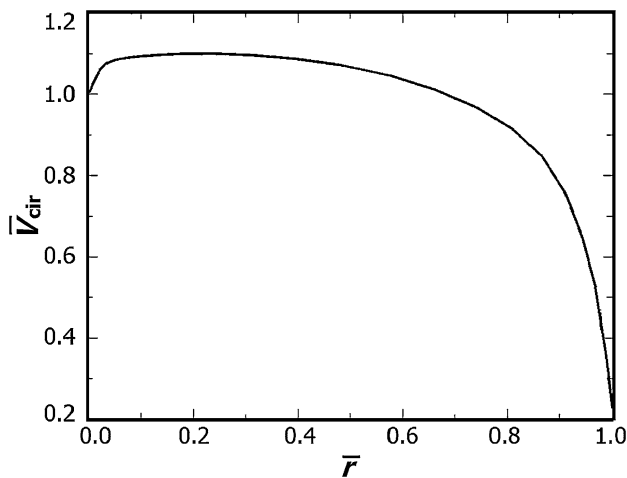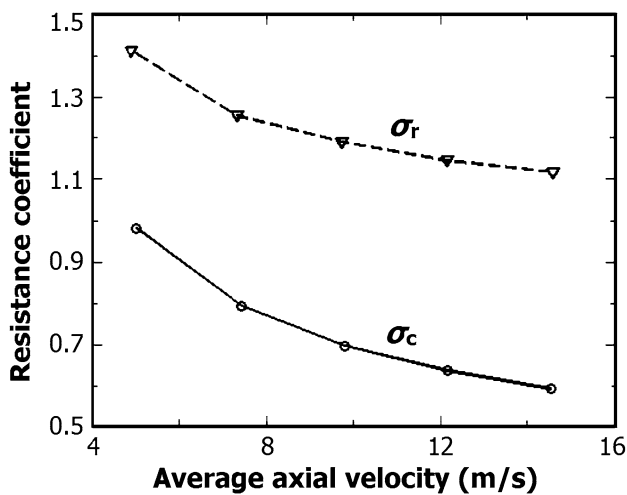

Fig. 5 Circumferential velocity along a *radial line* at seal inlet

Table 4 Average axial velocity and pressure drop

Seal	Inlet mass flow rate (kg/s)	Average axial velocity (m/s)	Pressure drop (MPa)
Plain	0.450	5.02	0.048
	0.675	7.43	0.085
	0.900	9.81	0.130
	1.125	12.18	0.183
	1.350	14.54	0.243
Tooth-on-stator seal	0.450	4.91	0.066
	0.675	7.34	0.131
	0.900	9.76	0.220
	1.125	12.19	0.330
	1.350	14.60	0.462

Fig. 6 Flow resistance coefficients
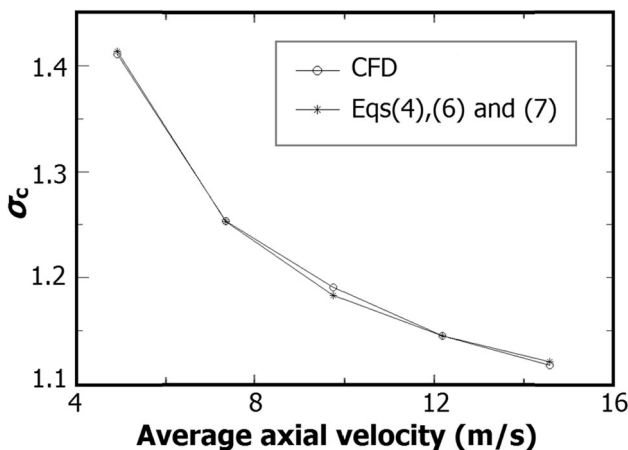
Fig. 7 σ_c values obtained by CFD and Eqs. (4), (6) and (7)

by Childs et al. [10] are Eqs. (17–19), being the first-order axial-momentum equation, the circumferential-momentum equation and the continuity equation, respectively, in their dimensionless forms.

$$\frac{\partial p_1}{\partial z} = h_1 A_{1z} - u_{\theta 1} A_{2z} - u_{z1} A_{3z} \\ - \left\{ \frac{\partial u_{z1}}{\partial \tau} + (\omega T) u_{\theta 0} \frac{\partial u_{z1}}{\partial \theta} + \frac{\partial u_{z1}}{\partial z} \right\}, \quad (17)$$

$$b_s \left(\frac{L}{r} \right) \frac{\partial p_1}{\partial \theta} = h_1 A_{1\theta} - u_{\theta 1} A_{2\theta} - u_{z1} A_{3\theta} \\ - \left\{ \frac{\partial u_{\theta 1}}{\partial \tau} + (\omega T) u_{\theta 0} \frac{\partial u_{\theta 1}}{\partial \theta} + \frac{\partial u_{\theta 1}}{\partial z} \right\}, \quad (18)$$

$$\frac{\partial u_{z1}}{\partial z} + (\omega T) \frac{\partial u_{\theta 1}}{\partial \theta} = - \left[(\omega T) u_{\theta 0} \frac{\partial h_1}{\partial \theta} + \frac{\partial h_1}{\partial \tau} \right], \quad (19)$$

where u, p and h, being all dimensionless, are the velocity component, and the pressure and radial clearance changes, respectively; the subscripts 0, 1, θ and z represent the zeroth-order value, the first-order value, the circumferential direction and the axial direction, respectively; and the other parameters are defined as follows [10].

$$A_{1z} = \frac{a_{0s}\sigma_s(1 - m_s) + a_{0r}\sigma_r(1 - m_r)}{2} \quad (20)$$

$$A_{2z} = \frac{(m_s + 1)\sigma_s a_{1s} u_{\theta 0} + (m_r + 1)\sigma_r a_{1r}(u_{\theta 0} - 1)}{2b_s^2} \quad (21)$$

$$A_{3z} = \frac{a_{0s}\sigma_s(2 + m_s) + a_{0r}\sigma_r(2 + m_r)}{2} \\ - \frac{(m_s + 1)\sigma_s a_{1s} u_{\theta 0}^2 + (m_r + 1)\sigma_r a_{1r}(u_{\theta 0} - 1)^2}{2b_s^2}$$

$$(22)$$

$$A_{1\theta} = \frac{a_{0s}\sigma_s(1 - m_s)u_{\theta 0} + a_{0r}\sigma_r(1 - m_r)(u_{\theta 0} - 1)}{2} \quad (23)$$

$$A_{2\theta} = \frac{\sigma_s a_{0s} + \sigma_r a_{0r}}{2} \\ + \frac{(m_s + 1)\sigma_s a_{1s} u_{\theta 0}^2 + (m_r + 1)\sigma_r a_{1r}(u_{\theta 0} - 1)^2}{2b_s^2} \quad (24)$$

$$A_{3\theta} = \frac{a_{0s}\sigma_s m_s u_{\theta 0} + a_{0r}\sigma_r m_r(u_{\theta 0} - 1)}{2} \\ - \frac{(m_s + 1)\sigma_s a_{1s} u_{\theta 0}^3 + (m_r + 1)\sigma_r a_{1r}(u_{\theta 0} - 1)^3}{2b_s^2} \quad (25)$$
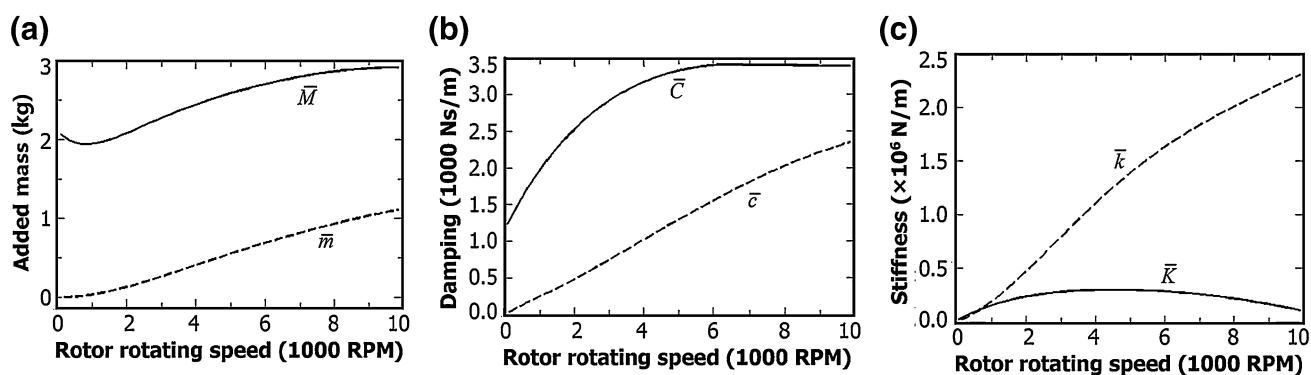
(a)
(b)
(c)

Fig. 8 Coefficients of added mass (**a**), damping (**b**) and stiffness (**c**)
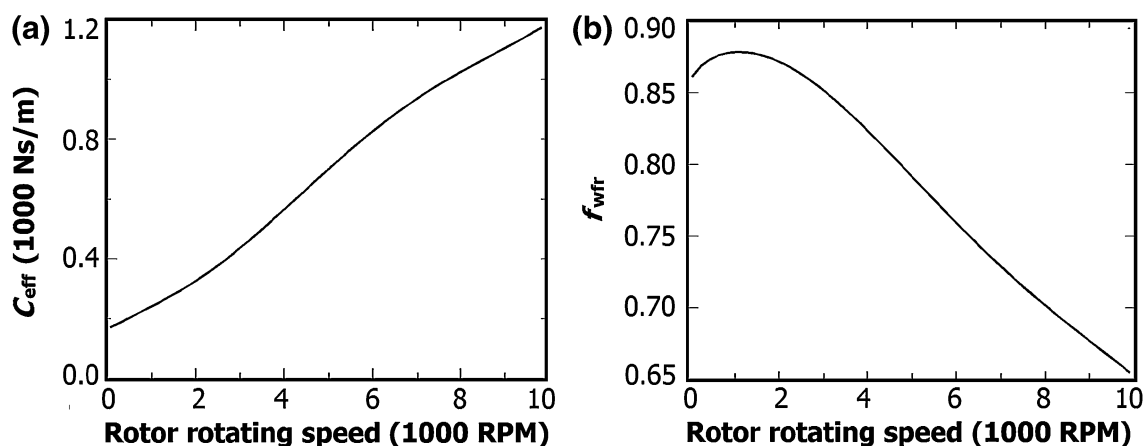
(a)
(b)

Fig. 9 Effective damping (**a**) and whirl frequency ratio (**b**)

$$a_{0s} = \frac{\left(1 + \left(\frac{u_{\theta 0}}{b_s u_{z0}}\right)^2\right)^{\frac{m_s+1}{2}}}{B_s}, \quad a_{0r} = \frac{\left(1 + \left(\frac{u_{\theta 0}-1}{b_s u_{z0}}\right)^2\right)^{\frac{m_r+1}{2}}}{B_r}$$

$$a_{1s} = \frac{\left(1 + \left(\frac{u_{\theta 0}}{b_s u_{z0}}\right)^2\right)^{\frac{m_s-1}{2}}}{B_s}, \quad a_{1r} = \frac{\left(1 + \left(\frac{u_{\theta 0}-1}{b_s u_{z0}}\right)^2\right)^{\frac{m_r-1}{2}}}{B_r}$$

(26)

$$B_s = \left(1 + \frac{1}{4b_s^2}\right)^{\frac{m_s+1}{2}}, B_r = \left(1 + \frac{1}{4b_s^2}\right)^{\frac{m_r+1}{2}}$$

(27)

All the dimensionless values are calculated by the following expressions.

$$u_z = \frac{U_z}{V_s}, u_\theta = \frac{U_\theta}{r\omega}, p = \frac{P}{\rho V_s^2}, h = \frac{H + \epsilon_e H_1}{H}, z = \frac{Z}{L}, \tau = \frac{t}{T},$$

$$T = \frac{L}{V_s},$$

(28)

where U_z, U_θ, P, H, Z and t are the axial velocity, circumferential velocity, the pressure, the radial clearance, the axial axis coordinate and the time, respectively.

The zeroth-order and first-order equations are solved by finite difference method. The fluid induced forces are calculated by integrating the perturbed pressure p_1 along the circumferential and the axial directions.

(3) The fluid induced forces are expressed as.

$$-\frac{f_n(\Omega T)}{\pi r \Delta p R_0} = \bar{K} + \bar{c}(\Omega T) - \bar{M}(\Omega T)^2,$$

(29)

$$\frac{f_t(\Omega T)}{\pi r \Delta p R_0} = \bar{k} - \bar{C}(\Omega T) - \bar{m}(\Omega T)^2,$$

(30)

where R_0 is the amplitude of the rotor whirl motion; $T = L/V_s$ is the time elapsed of a fluid element flowing through the seal axially; $\bar{M}$, $\bar{m}$, $\bar{C}$, $\bar{c}$, $\bar{K}$ and $\bar{k}$ are rotordynamic coefficients in their dimensionless forms; and Ω is the whirl frequency, on which the fluid induced forces are depended. The rotordynamic coefficients are calculated in a range of rotating speeds, denoted as ω. For each ω, five Ω values are specified. This provides enough number of fluid induced forces for every ω to be fitted into Eqs. (29) and (30). Then the corresponding rotordynamic coefficients are obtained.
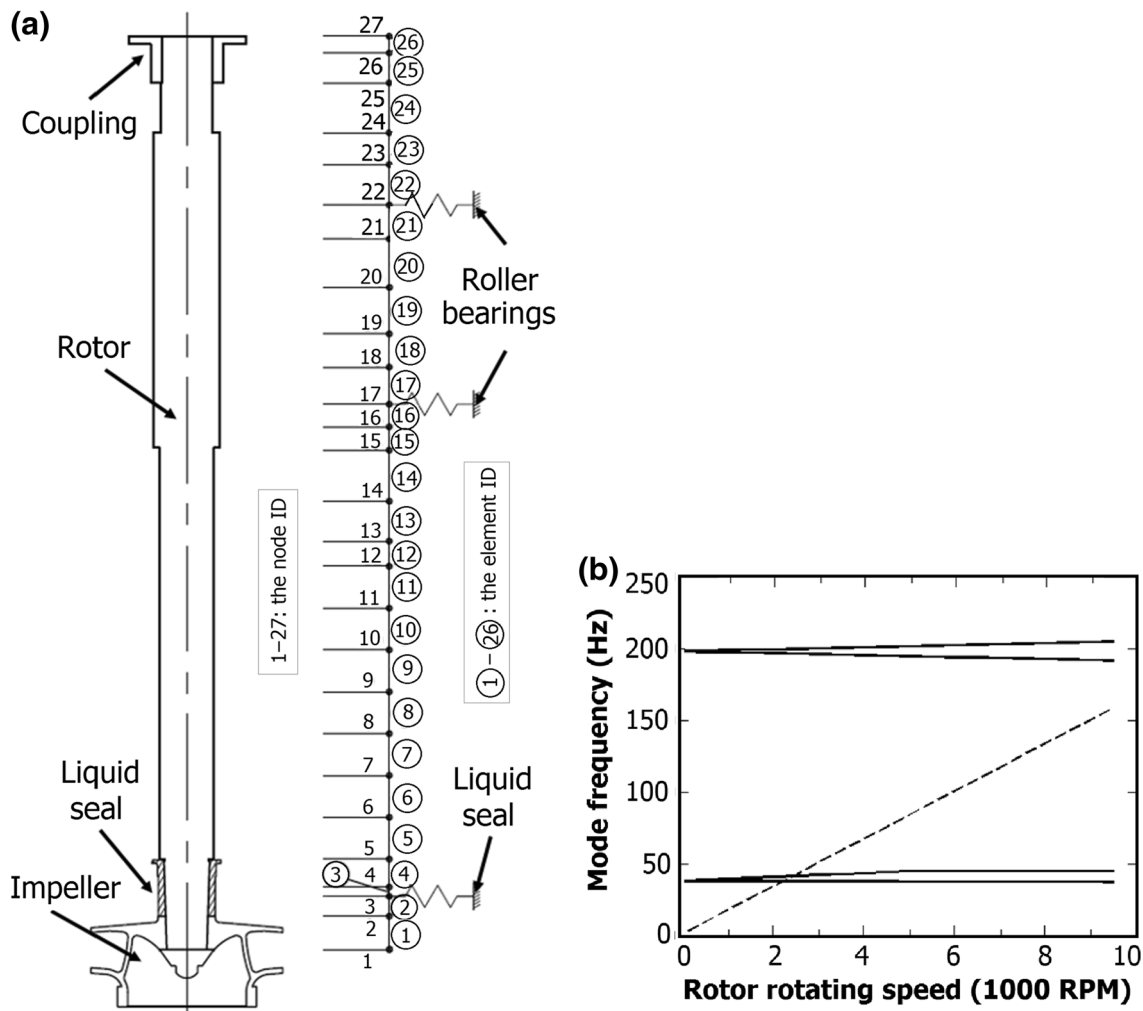
🖄 Springer

Fig. 10 Rotordynamic model (**a**) and the Campbell diagram (**b**)

5 Results and discussion

Rotordynamic coefficients of the added mass, damping and stiffness are shown in Fig. 8. Both the direct and cross-coupled added mass coefficients are significantly larger than the fluid mass displaced by the rotor. The added mass coefficients approximately equal the weight of the adjacent rotor segment. Therefore, the added mass should be considered in future rotordynamic analysis. The damping affects the pump stability since the liquid seal is a main source of external damping. This is of significant importance when the rotor is supported by roller bearings instead of fluid film bearings, because little damping effect can be generated by the roller bearings. As shown in Fig. 8c, the liquid seal brings both direct and cross-coupled stiffness into the rotor system. The cross-coupled stiffness decreases the overall stability. The results in Fig. 8c mean that the liquid seal introduces considerable cross-coupled stiffness and its value increases with rotating speed. Besides, the

direct stiffness may drop below zero over 10,000 RPM, indicating that no positive contribution can be expected from stiffness if the rotor is operating at this speed or beyond. Similar phenomena were observed recently by Vannini et al. [21] in their experimental tests on a labyrinth gas seal with positive pre-swirl.

Effects of liquid seal on stability of the rotor system can be investigated by examining the effective damping, $C_{eff} = C - k/\omega$, and whirl frequency ratio, $f_{wfr} = k/(C\omega)$ [22]. The results are shown in Fig. 9. One sees that the C_{eff} remains positive in the speed range concerned in this study. This may be due to that the seal can still bring stabilizing effect, despite the increase in cross-coupled stiffness. The f_{wfr} curve also shows that the stabilizing effect exists while the rotating speed is increasing.

In order to study stability and safety of the pump and examine how the liquid seal affect the rotordynamic characteristics of the pump, a preliminary rotordynamic analysis is performed. A simple lumped-mass model is

**Table 5** Geometry of the rotordynamic model

Element no.	Diameter (m)	Length (m)	Element no.	Diameter (m)	Length (m)
1	0.06	0.05	14	0.08	0.077
2	0.06	0.03	15	0.1	0.035
3	0.06	0.014	16	0.1	0.034
4	0.06	0.042	17	0.1	0.056
5	0.08	0.063	18	0.1	0.05
6	0.08	0.063	19	0.1	0.07
7	0.08	0.063	20	0.1	0.073
8	0.08	0.063	21	0.1	0.051
9	0.08	0.063	22	0.1	0.061
10	0.08	0.063	23	0.1	0.048
11	0.08	0.063	24	0.075	0.075
12	0.08	0.038	25	0.075	0.045
13	0.08	0.06	26	0.075	0.025

Table 6 Inertia information of the components installed on the rotor

Component	Node ID	Mass (kg)	Moment of inertia (kg m^2)	
			Polar	Diametrical
Impeller	1	15.0	0.078	0.120
Coupling	26	4.0	0.013	0.016

built in the environment of Ansys APDL software. Figure 10a shows schematically the rotordynamic model. The rotor is discretized into 26 beam elements. The geometry parameters are listed in Table 5. The mass point elements are used to represent the impeller and the coupling, and their parameters are given in Table 6. The roller bearings are approximated by linearized stiffness coefficients and are modeled by the spring elements provided by the software. The stiffness of the roller bearings is 8×10^7 N/m. No damping effects are provided by the roller bearings. The rotordynamic coefficients of the liquid seal are described by tables in Ansys APDL. The rotordynamic coefficients of a specific rotating speed are obtained by interpolation between the nearest two values stored in the tables. The computed first critical speed of the pump rotor without the liquid seal is 2304 RPM, but it goes up to 2468 RPM if the liquid seal is considered. The resulting Campbell diagram considering the liquid seal is shown in Fig. 10b, where the dashed line represents the frequency of the rotating speed.

In order to get more insight into the dynamic characteristics of the molten salt pump, an unbalance harmonic response analysis is performed. The unbalance force of 0.0015 kg·m is applied on Node 1 of the finite element model in Fig. 10a. The result is shown in Fig. 11, where the displacement amplitude of Node 1 is drawn against the rotating speed with step size of 10 RPM. The response
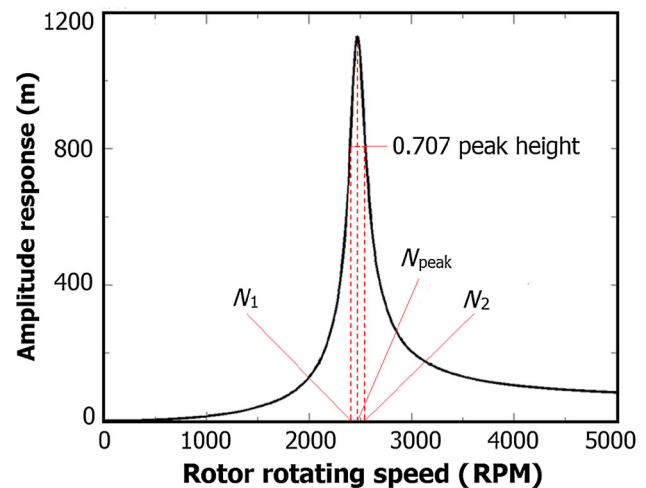
Fig. 11 Unbalance harmonic response

reaches the peak value at the rotating speed (N_{peak}) around the first critical speed. N_1 and N_2 denote the threshold frequencies of the half-power region. The amplification factor is $AF = N_{peak}/(N_2 - N_1) = 16.6$, indicating that the rotor is sensitive to unbalance force and it should not operate at speeds near the first critical speed [23]. If the maximum continuous operating speed of the pump is 125 % of the design point, which is 1450 RPM, the separation margin of the first critical speed is about 36 %. Since the molten salt pump is designed to operate under the first critical speed, this separation margin is still enough for the pump to operate safely.

6 Conclusion

Aimed at analyzing rotordynamic coefficients of the liquid seal in a molten salt pump, the inlet pressure loss and inlet pre-swirl are obtained by CFD technique. The

resistance of liquid seal is analyzed by CFD method. Successive simulations determine the wall coefficients. Rotordynamic coefficients of the seal are estimated, and further rotordynamic analysis is performed. The main results are summarized as follows:

(1) Significant inlet pre-swirl exists in the current design of the molten salt pump.

(2) The seal resistance can be well predicted using the obtained wall coefficients, in certain range of seal leakage.

(3) The added mass produced by the liquid seal is of the same magnitude with the nearby rotor segment. The mass coefficients should be considered in dynamics analysis of the rotor system.

(4) In the range of operating speeds, the damping and direct stiffness coefficients are positive. The liquid seal brings significant destabilizing cross-coupled stiffness. However, the effective damping and whirl frequency ratio indicate that the destabilizing effect is limited. Further rotordynamic analysis of the molten salt pump shows that separation margin of the first critical speed is still enough for the pump to operate under the designed point.

References

1. R. Fritz, The effects of an annular fluid on the vibrations of a long rotor, Part 1 theory. J. Fluid Eng.-T ASME **92**, 923–929 (1970). doi:10.1115/1.3425165

2. R. Fritz, The effects of an annular fluid on the vibrations of a long rotor, Part 2 ttest. J. Fluid Eng.-T ASME **92**, 930–937 (1970). doi:10.1115/1.3425166

3. D.W. Childs, Finite-length solutions for rotordynamic coefficients of turbulent annular seals. J. Tribol. **105**, 437–444 (1983). doi:10.1115/1.3254636

4. G.G. Hirs, A Bulk-flow theory for turbulence in lubricant films. J. Tribol. **95**, 137–145 (1973). doi:10.1115/1.3451752

5. D.L. Rhode, S.J. Hensel, M.J. Guidry, Labyrinth seal rotordynamic forces using a 3-D Navier-Stokes code. J. Tribol. **114**, 683–689 (1992). doi:10.1115/1.2920936

6. M.M. Athavale, R.C. Hendricks, B.M. Steinetz, in *Numerical simulation of flow in a whirling annular seal and comparison with experiments*, the 31st Joint Propulsion Conference and Exhibit, San Diego, California, United States, Jul. 10–12, 1995

7. J.J. Moore, A.B. Palazzolo, CFD Comparison to 3D laser anemometer and rotordynamic force measurements for grooved liquid annular seals. J. Tribol. **121**, 306–314 (1999). doi:10.1115/1.2833937

8. J.J. Moore, 3-D CFD rotordynamic analysis of gas Labyrinth seals. J. Vib. Acoust. **125**, 427–433 (2003). doi:10.1115/1.1615248

9. A. Untaroiu, V. Hayrapetian, C.D. Untaroiu et al., On the dynamic properties of pump liquid seals. J. Fluids Eng. **135**, 051104 (2013). doi:10.1115/1.4023653

10. D.W. Childs, C.H. Kim, Analysis and testing for rotordynamic coefficients of turbulent annular seals with different, directionally-homogeneous surface-roughness treatment for rotor and stator elements. J. Tribol. **107**, 296–305 (1985). doi:10.1115/1.3261054

11. G.F. Kleynhans, D.W. Childs, The acoustic influence of cell depth on the rotordynamic characteristics of smooth-rotor/honeycomb-stator annular gas seals. J. Eng. Gas Turbines Power **119**, 949–956 (1997). doi:10.1115/1.2817079

12. C.G. Holt, D.W. Childs, Theory versus experiment for the rotordynamic impedances of two hole-pattern-stator gas annular seals. J. Tribol. **124**, 137–143 (2002). doi:10.1115/1.1398297

13. D.W. Childs, S. Arthur, N.J. Mehta, The impact of hole depth on the rotordynamic and leakage characteristics of hole-pattern-stator gas annular seals. J. Eng. Gas Turbines Power **136**, 042501 (2014). doi:10.1115/1.4025888

14. P.J. Migliorini, A. Untaroiu, H.G. Wood et al., A computational fluid dynamics/bulk-flow hybrid method for determining rotordynamic coefficients of annular gas seals. J. Tribol. **134**, 022202 (2012). doi:10.1115/1.4006407

15. M.S. Sohal, M.A. Ebner, P. Sabharwall et al., *Engineering Database of Liquid Salt Thermophysical and Thermochemical Properties* (Idaho National Laboratory, Idaho Falls, 2010)

16. I.B. Celik, U. Ghia, P.J. Roache, Procedure for estimation and reporting of uncertainty due to discretization in CFD applications. J. Fluids Eng. **130**, 078001 (2008). doi:10.1115/1.2960953

17. D.W. Childs, P. Fayolle, Test results for liquid "damper" seals using a round-hole roughness pattern for the stators. J. Tribol **121**, 42–49 (1999). doi:10.1115/1.2833809

18. W.T. Lindsey, D.W. Childs, The effects of converging and diverging axial taper on the rotordynamic coefficients of liquid annular pressure seals: theory versus experiment. J. Vib. Acoust. **122**, 126–131 (2000). doi:10.1115/1.568457

19. M.K. Gupta, D.W. Childs, Rotordynamic stability predictions for centrifugal compressors using a bulk-flow model to predict impeller shroud force and moment coefficients. J. Eng. Gas Turbines Power **132**, 091402 (2010). doi:10.1115/1.2720519

20. T. Staubli, M. Bissig, in *Numerically calculated rotor dynamic coefficients of a pump rotor side space*, International Symposium on Stability Control of Rotating Machinery (ISCORMA), South Lake Tahoe, California, United States, Aug. 20–24, 2001

21. G. Vannini, S. Cioncolini, G.D. Vescovo et al., Labyrinth seal and pocket damper seal high pressure rotordynamic test data. J. Eng. Gas Turbines Power **136**, 022501 (2014). doi:10.1115/1.4025360

22. N.J. Mehta, D.W. Childs, Measured Comparison of leakage and rotordynamic characteristics for a slanted-tooth and a straight-tooth labyrinth seal. J. Eng. Gas Turbines Power **136**, 012501 (2014). doi:10.1115/1.4025267

23. Standard Paragraphs A P I. Publication 684, Tutorial on the API Standard Paragraphs Covering Rotor Dynamics and Balancing: An Introduction to Lateral Critical and Train Torsional Analysis and Rotor Balancing, American Petroleum Institute, February 1996